The electron forewake: Shadowing and drift-energization as flowing magnetized plasma encounters an obstacle

PSFC/JA-15-33

The Electron Forewake: Shadowing and Drift-Energization as Flowing Magnetized Plasma Encounters an Obstacle

C.B. Haakonsen and I.H. Hutchinson

July 2015

Plasma Science and Fusion Center
Massachusetts Institute of Technology
Cambridge MA 02139 USA

This work was supported by the U.S. Department of Energy, Grant No. DE-FG02-06ER54891.

Submitted to *Physics of Plasmas.*

The Electron Forewake: Shadowing and Drift-Energization as Flowing Magnetized Plasma Encounters an Obstacle

Christian Bernt Haakonsen[1, a)] and Ian H. Hutchinson[1, b)]
Plasma Science and Fusion Center, Massachusetts Institute of Technology, Cambridge, Massachusetts 02139, USA

(Dated: 21 July 2015)

Flow of magnetized plasma past an obstacle creates a traditional wake, but also a forewake region arising from shadowing of electrons. The electron forewakes resulting from supersonic flows past insulating and floating-potential obstacles are explored with 2D electrostatic particle-in-cell simulations, using a physical ion to electron mass ratio. Drift-energization is discovered to give rise to modifications to the electron velocity-distribution, including a slope-reversal, providing a novel drive of forewake instability. The slope-reversal is present at certain locations in all the simulations, and appears to be quite robustly generated. Wings of enhanced electron density are observed in some of the simulations, also associated with drift-energization. In the simulations with a floating-potential obstacle, the specific potential structure behind that obstacle allows fast electrons to cross the wake, giving rise to a more traditional shadowing-driven two-stream instability. Fluctuations associated with such instability are observed in the simulations, but this instability-mechanism is expected to be more sensitive to the plasma parameters than that associated with the slope-reversal.

PACS numbers: 52.30.-q, 52.35.Fp, 52.35.Mw, 52.35.Qz, 52.35.Qz, 52.35.Tc, 52.65.Rr, 95.30.Qd, 96.20.-n, 96.25.Qr, 96.25.St, 96.50.Ci

I. INTRODUCTION

The study of magnetized plasma flow past non-magnetic obstacles has wide applicability, ranging from the interaction of the solar wind with the Moon[1] to Mach probe measurements in Tokamaks[2]. A typical configuration is a fully ionized uniform background plasma with an $\mathbf{E}\times\mathbf{B}$ drift perpendicular to the magnetic field, or the equivalent perpendicular obstacle motion. Different parallel and perpendicular drift speeds give rise to a wide range of wake structures and phenomena, which also depend on the nature of the obstacle, the strength of the magnetic field, the plasma Debye length, and the ion and electron temperatures. The parameter space of interest is thus vast, but targeted simulations such as those presented in this paper can discover and reveal the nature of the various phenomena in specific regions of that space.

To model the solar wind wake behind the Moon, extensive hybrid simulations have previously been carried out using simplified (typically fluid) electron models[3–8], but simulations with kinetic electrons[9–13] have identified important phenomena not captured by such hybrid treatments. In particular, it was recently shown in kinetic 1D simulations[13] that the lunar wake may be unstable much closer to the Moon than expected from hybrid simulations. Drift de-energization[14], where the parallel kinetic energy of some electrons change as the result of $\mathbf{E}\times\mathbf{B}$ drifts induced by the wake potential structure, plays an important role in that instability[15].

Just as de-energization takes place in the wake, drift energization can take place when flowing plasma encounters an electron-repelling obstacle. The energizing drift is in that case driven by gradients of the potential structure near the obstacle, but is analogous to the more commonly studied case of drift driven by magnetic field gradients at a shock[16–18]. Such magnetically driven energization gives rise to an electron *foreshock* at the Earth's bow shock[19], encompassing electron beams and various instability-driven fluctuations[20,21], so one might expect to see similar phenomena resulting from electron energization as flow encounters an unmagnetized obstacle. Fluctuations reminiscent of those seen in the foreshock have indeed been observed ahead of the lunar wake[22], and the term *forewake* suggested for that region. The fluctuations have been proposed to be the result of *shadowing*[23,24], which predicts an unstable gap in the electron distribution on field lines down-stream of the rear-end of the obstacle. It is shown in the present work that including the effects of space-charge and the surface potential of the obstacle can give rise to more elaborate (and likely unstable) perturbations to the electron distribution function than expected from shadowing alone, potentially driving various instabilities in the forewake region far upstream of the traditional (ion) wake; *forewake* is used here to refer in general to such a region, unspecific to the nature of the obstacle.

Fluid theory and hybrid simulations have also been used extensively to study transverse Mach probes[25–33], where relating plasma flow to particle fluxes to the probe's electrodes is of particular interest. Attention to kinetic electron effects has so far been limited to correcting the electron flux to a spherical collector[34] in hybrid magnetic simulations, but understanding the impact of such effects will be of increasing importance as the models used to interpret probe signals become more sophis-

[a)] chaako@mit.edu
[b)] ihutch@mit.edu

ticated, for instance by including the effects of inhomogeneities in the background plasma[29]. Typically being negatively biased, Mach probes are expected to cause drift energization of electrons, thereby creating a forewake which could potentially affect probe measurements. Only insulating and floating-potential conducting obstacles are considered in the present work, but both are found to lead to drift energization and electron distributions with reversed slopes that are expected to be unstable; in the conducting case instability is indeed observed, though seemingly as the result of an additional distribution feature from electrons passing behind the obstacle.

This paper is organized as follows: The 2D electrostatic simulation approach used is described in Section II. Ballistic simulations are used to illustrate the effect of shadowing in Section III, establishing a basis for comparison. Simulations of plasma flow past an insulating obstacle with a circular cross-section are presented in Section IV, showing the effects of space-charge and the locally varying surface potential of the obstacle. Flow past a floating-potential conducting cylinder is then explored in Section V, and is found to be unsteady for both drift speeds simulated. Implications of the present results are discussed in Section VI, and some concluding remarks given in Section VII.

II. 2D ELECTROSTATIC SIMULATION METHOD

A stationary obstacle with circular cross-section is taken to obstruct flow in a fully ionized hydrogen plasma with a uniform background magnetic field. In this frame the perpendicular component of plasma flow is $\mathbf{E}\times\mathbf{B}$ drift, but it could equivalently be a stationary plasma with a moving obstacle. There are two main computational approaches to simulating such a configuration: fully kinetic methods like particle-in-cell (PIC), and hybrid methods that use simplified models for the electrons. Kinetic treatment of the electrons is computationally expensive, especially when considering the true ion to electron mass ratio ($m_\mathrm{i}/m_\mathrm{e} = 1836$ for hydrogen), limiting the feasible dimensionality and resolution of such simulations. Hybrid methods are a useful way to relax those limitations and study large multi-dimensional systems, but can only include certain classes of (typically fluid) electron phenomena. Exploring the importance of true kinetic electron effects thus requires a fully kinetic treatment, and the present simulations have been enabled by an upgrade of the COPTIC code[35] to allow for kinetic (rather than Boltzmann) electrons.

COPTIC is a three-dimensional electrostatic PIC code with Cartesian coordinates, but can model 2D geometries using periodicity (and few grid cells) in one dimension. That is the mode used for the present simulations, where the y-dimension is made periodic such that the drift and spatial variation are in the x–z plane. The uniform magnetic field is taken to be aligned with the z-axis, such that the background $\mathbf{E}\times\mathbf{B}$ drift $\mathbf{v}_\mathrm{d}$ is along the (negative) x-axis. This gives a drifting Maxwellian background distribution for both the ions and electrons, taken to have the same drift and temperature ($T_\mathrm{i} = T_\mathrm{e}$). Rather than resolve the gyromotion of the particles, their parallel motion is advanced with a standard leap-frog scheme[36], while the perpendicular motion is taken to be the imposed drift. The present simulations are thus the natural 2D extension of 1D kinetic wake simulations[9–13], correctly accounting for the extent of the obstacle and potential variation in the flow-direction. Ignoring the electron gyromotion is appropriate when the electron gyrofrequency is much greater than the electron plasma frequency ($\omega_\mathrm{ce} \gg \omega_\mathrm{pe}$), but that does not guarantee that the ion gyroradius is small compared to the scale of perpendicular potential variation. However, for supersonic drifts the ion gyromotion is only a perturbation to the drift, so simulations at weaker magnetic fields where the ion gyroradius is larger than the Debye length are not expected to differ drastically from those presented here.

All the present simulations are conducted at the true mass ratio for hydrogen, and at a background electron Debye length $\lambda_\mathrm{De} = {}^{R_\mathrm{o}}/_{16}$ (except in Section III), where R_o is the radius of the circular cross-section of the obstacle. This Debye length is chosen to be much smaller than the size of the obstacle, while still being large enough for simulations with acceptable noise levels to be computationally feasible with COPTIC. Except where otherwise noted, the computational domain is taken to be centered on the obstacle and extend from $-2R_\mathrm{o}$ to $2R_\mathrm{o}$ in the x-direction and from $-16R_\mathrm{o}$ to $16R_\mathrm{o}$ in the z-direction, subdivided into 256 and 2048 grid-cells respectively. The drift is taken to be directed towards negative x, and to have magnitude of either $8c_\mathrm{s}$ or $32c_\mathrm{s}$; both are firmly supersonic, and the latter is approaching the electron thermal speed ($43c_\mathrm{s}$). Roughly 3×10^7 particles of each species are moved, using a time-step $dt = {}^{R_\mathrm{o}}/_{2048c_\mathrm{s}}$ such that a thermal electron takes multiple time-steps to cross a Debye length.

The obstacle is taken to either have a uniform potential ϕ_o across its surface (as a conductor would), or to have a spatially varying potential which balances the electron and ion currents to each of 256 segments of its surface (as an insulator would); in the case of the uniform potential it is adjusted to find the floating potential, for which the total ion and electron currents to the obstacle balance. Whether for the whole obstacle or an individual facet, the potential adjustment is made based on the electron and ion flux to that segment over the past time-step, smoothing that adjustment over 64 time-steps, which is longer than the typical time-scale for plasma oscillations but short enough for the potential to settle well before the end of the simulation (2048 time-steps). In the case of zero ion and electron flux in a given time-step to a facet within a ${}^{\pi}/_{4}$ angle of the center of the wake, the adjusted potential (before temporal smoothing) is taken to be the current potential of the facet closest to but outside that angle range.

As boundary conditions for the potential, one of two

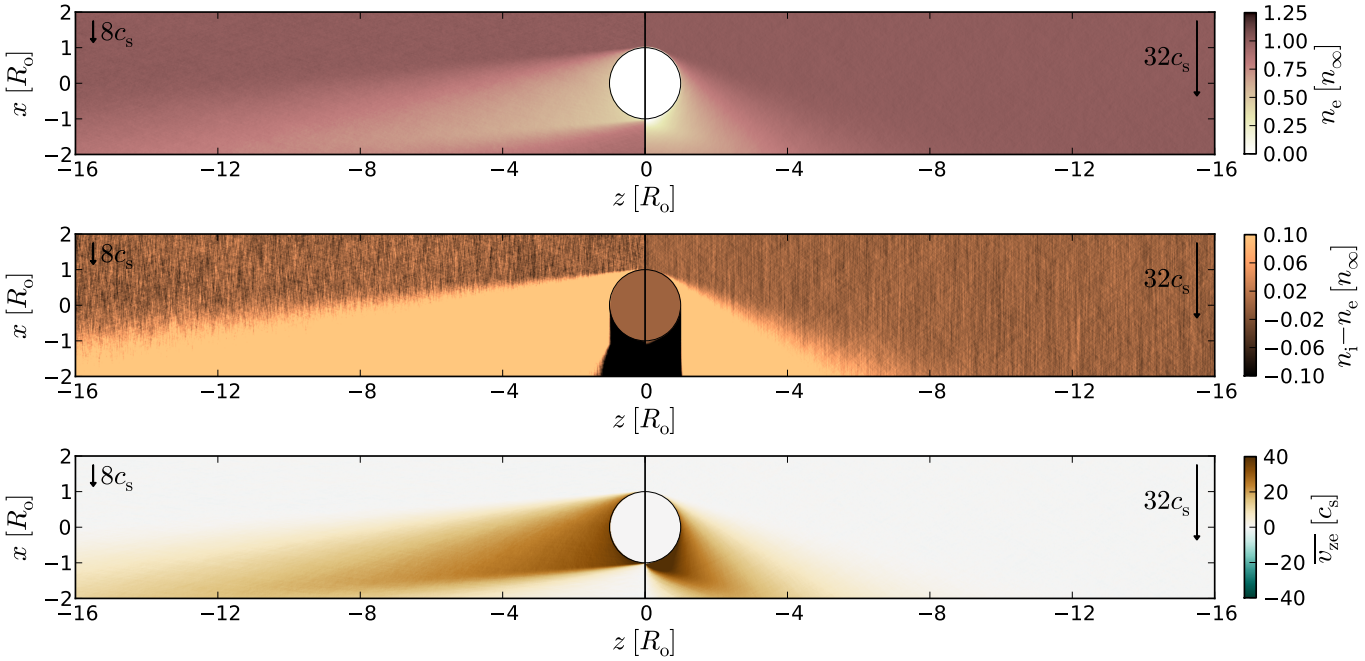

FIG. 1. Shadowing by an uncharged ($\phi_o = 0$) obstacle in a tenuous ($\lambda_{De} = \infty$) plasma, showing the resulting electron density n_e, normalized charge density $n_i - n_e$, and average parallel electron velocity $\overline{v_{ze}}$ for drift speeds $8c_s$ (left) and $32c_s$ (right, with inverted z-axis). Color scales are saturated in some regions.

types is selected for each boundary perpendicular to one of the non-periodic axes. The first, Neumann zero-normal-gradient boundary condition, is used for the boundary through which the drifting plasma leaves the computational domain. The second, Dirichlet zero-potential boundary condition, is used for the remaining three non-periodic boundaries. This latter choice may become inaccurate at slow drift speeds, if potential perturbations and electrons that have interacted with the obstacle make it to the boundaries perpendicular to the magnetic field. However, such inaccuracy does not appear to be significant for the present simulations.

III. SHADOWING

Ballistic particle motion, unaffected by electric fields, is considered here by simulating an uncharged obstacle ($\phi_o = 0$) in a tenuous ($\lambda_{De} = \infty$) plasma. This leaves shadowing as the only influence of the obstacle on the plasma, and the resulting electron density, charge density, and average parallel electron velocity are shown in Figure 1. Since the drift is perpendicular to the magnetic field, the simulations are symmetric about $z = 0$, so only the $z < 0$ half of the domain is shown for each of the two drift speeds ($8c_s$ and $32c_s$). The electron density is depleted in the shadowed region, and the average parallel velocity is towards the obstacle because some outward-going trajectories are unpopulated; the electron thermal speed can be exceeded (and color-scale saturated) in some regions behind the obstacle because only the fastest particles in one directions make it there. For $x < -R_o$ some electrons passing behind the obstacle are present, leading to less electron-density depletion and an unstable electron distribution[23]. There are almost no ions immediately behind the obstacle, so the electrons that make it there lead to a negative charge density, in contrast to the positive charge density elsewhere in the electron shadow. However, as pointed out in the previous work on shadowing[23], a shortcoming of ballistic treatments is that they do not self-consistently include the effects of such space-charge.

Though more computationally efficient methods exist for ballistic calculations, Figure 1 was generated using a full simulation to allow for the most convenient comparison with the other simulations presented in this paper. Since the only parameters changed were the Debye length and the obstacle potential, Figure 1 also illustrates the level of underlying particle noise in the simulations, independent of any plasma oscillations or other fluctuations. Except where otherwise noted, all plots of densities and average parallel velocities have been averaged over 128 time-steps, so the actual noise-level in a given time-step is significantly larger than that in the figures. However, all potentials and parallel electric fields shown in later figures are for a single time-step, indicating that spatially averaged on the local Debye-scale particle noise does not appear to have a large impact on the simulations. Vertical streaks are present in the charge-density because the ions do not move far enough in 128 time-steps to smooth out local density-variations arising from noise.

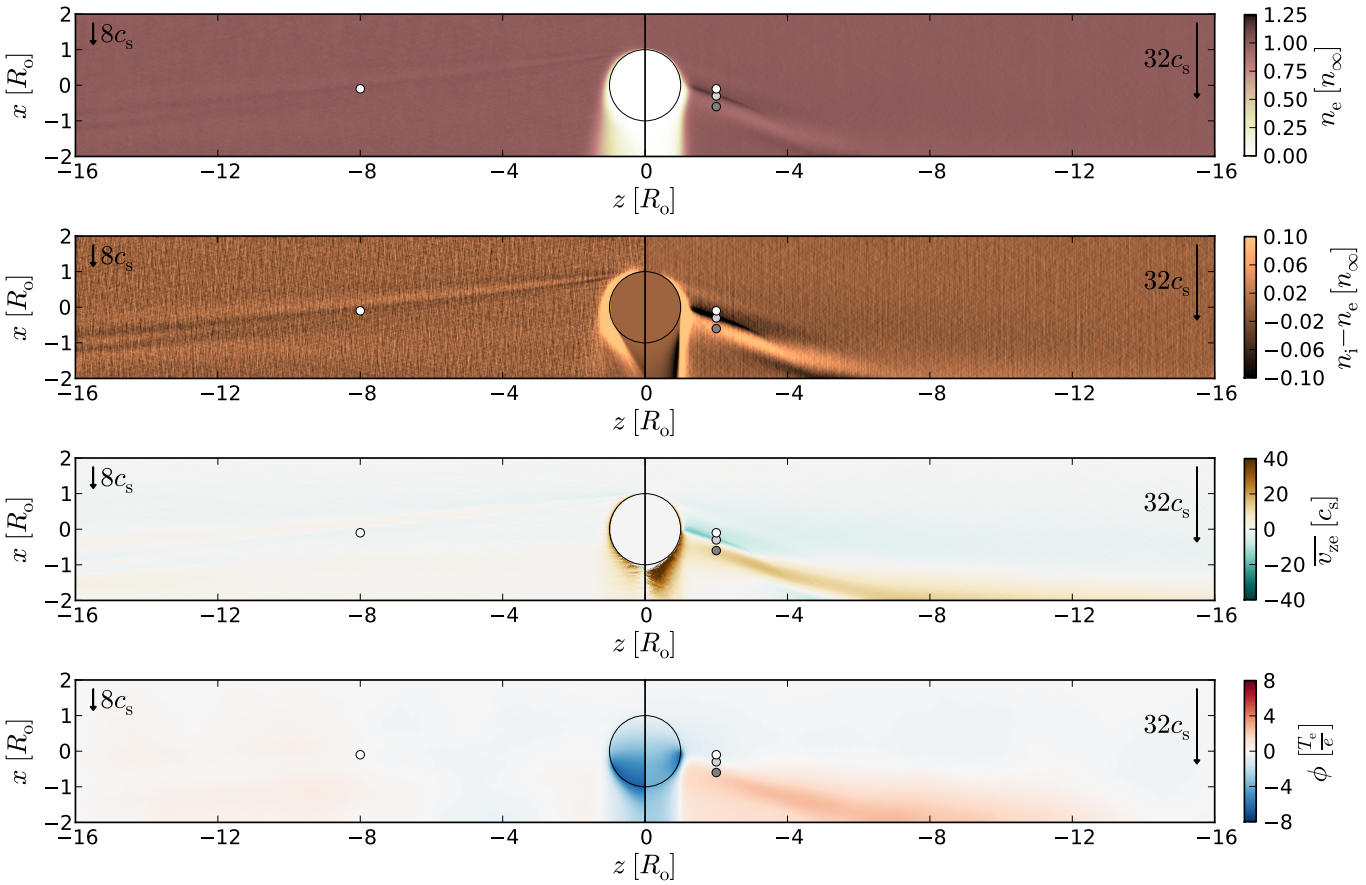

FIG. 2. Dense plasma ($\lambda_{De} = R_o/16$) drifting past an insulating obstacle, showing the electron density n_e, normalized charge density $n_i - n_e$, average parallel electron velocity $\overline{v_{ze}}$, and electrostatic potential ϕ for drift speeds $8c_s$ (left) and $32c_s$ (right). Small circles indicate locations for which the electron distribution is shown in later figures.

IV. INSULATING OBSTACLE

An insulating obstacle has conductivity small enough that charge does not redistribute on its surface, and will charge to a locally varying surface potential as discussed in Section II. The circular cross-section considered here is applicable for example to long insulating cylinders, or to insulating spheroids where the gyromotion scale is small compared to that of the obstacle in the direction of the background electric field.

A simulation with drift speed $8c_s$ and background electron Debye length $\lambda_{De} = R_o/16$ (used for all subsequent simulations) gives the electron density, charge density, average electron parallel velocity, and potential shown in the left half of Figure 2. Comparison with Figure 1 reveals that space-charge and surface-charging almost entirely replenish the electron density in the shadowed region to the side of the obstacle, also giving near-zero average parallel velocity there. An additional region of depleted electron-density is seen to arise immediately behind the obstacle, since the electron density cannot differ drastically from the ion density in the ion shadow, thus forming the traditional (ion) wake. As seen from the electrostatic potential the obstacle surface potential gradually transitions from zero at the top of the obstacle to a moderately negative value at the terminator, where the flow is tangential to the surface. This is because the ion flux (dominated by the flow) to the surface decreases as the angle between the flow and the surface changes, while the electron flux (dominated by thermal motion) would tend to increase; a negative surface potential is needed to reflect enough electrons to balance the local particle fluxes. Below the terminator the surface potential quickly becomes negative enough to repel almost all electrons, since only the very fastest ions make it to the back-side of the obstacle.

Though in the simulation the density is barely perturbed in what would otherwise be the electron shadow, the distribution is far from the background Maxwellian in some regions. The distribution at the left (drift speed $8c_s$) small white circle (at $x = -0.1R_o$ and $z = -8.0R_o$) in Figure 2 is shown in Figure 3, averaged over a box of width equal to the background electron Debye length in both x and z, and over 128 time-steps. To correct the error-bars for the fact that many particles do not cross the width of the distribution-box (λ_{De}) in either dimension in a single time-step (dt), the Gaussian counting error for a velocity-bin centered at parallel velocity v_b (and

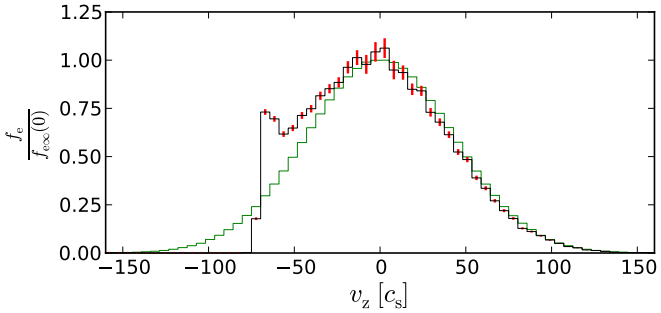

FIG. 3. Parallel electron velocity distribution f_e (black with red error bars) at the left (drift speed $8c_s$) small white circle (at $x = -0.1R_o$ and $z = -8.0R_o$) in Figure 2, and the background distribution (green).

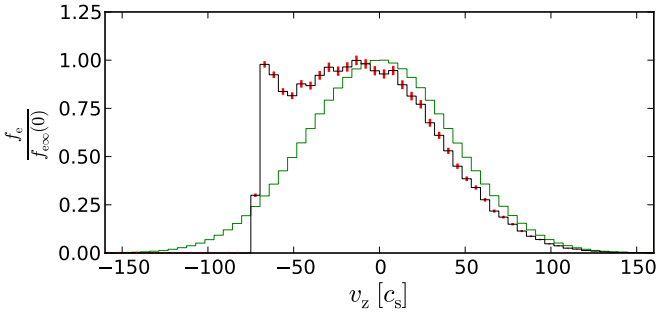

FIG. 4. Parallel electron velocity distribution f_e (black with red error bars) at the right (drift speed $32c_s$) small white circle (at $x = -0.1R_o$ and $z = -2.0R_o$) in Figure 2, and the background distribution (green).

drift speed v_d) has been divided by $\sqrt{\max(|v_b|, v_d)\, dt/\lambda_{De}}$, provided that factor is between $1/\sqrt{128}$ and 1. A factor less than $1/\sqrt{128}$ indicates that a single (very slow) particle has likely been counted 128 times, and so the correction factor is taken to be $1/\sqrt{128}$, while a factor greater than 1 indicates that all (fast) particles cross the width of the box in less than one time-step, so no correction is needed. The most striking feature of the distribution shown in Figure 3 is the cutoff at $v_z \approx -70c_s$, similar to that known to be present in the purely shadowed distribution, where it occurs at $v_z \approx -59c_s$ (at this location). The difference in cutoff-location implies that there has been parallel acceleration of some electrons away from the obstacle, which is also seen to have led to a reversal in slope of the distribution and a much higher value than the background distribution at the same velocity; this is discussed and illustrated with example particle trajectories in later figures. At slower speeds and for velocities toward the obstacle the distribution is largely unperturbed, though seemingly shifted slightly towards negative velocities. That shift indicates the presence of a large-scale electric field repelling electrons from the obstacle, presumably arising to remove any residual parallel electron velocity associated with the cutoff in the distribution (so that the electron density remains close to the ion one).

Looking closely at the left part of Figure 2, a narrow region of slightly depleted electron-density is seen to extend from the top of the obstacle. In this region the electron distribution is very similar to that resulting purely from shadowing, and it is when transitioning down into the region where the density recovers that distributions such as that shown in Figure 3 are present. The shadowing-like velocity-cutoff and reversed slope of the distribution quickly go away farther down, tending towards a Maxwellian distribution with a cutoff at more negative velocities. This shift of the cutoff arises because reflected particles replace most of the shadowed ones, and increasingly energetic electrons can be reflected farther down on the obstacle (where the potential is more negative).

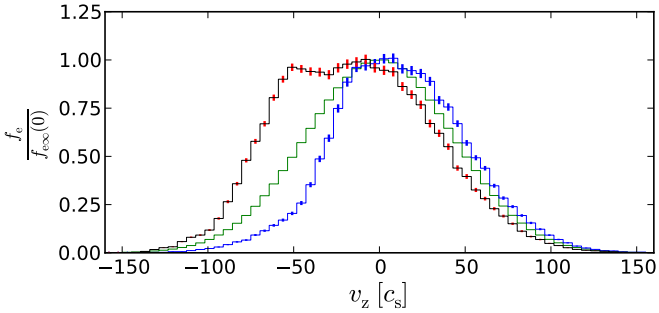

FIG. 5. Parallel electron velocity distribution f_e at the small light-gray circle in Figure 2 ($x = -0.3R_o$ and $z = -2.0R_o$; black with red error bars), and at the small dark-gray circle ($x = -0.6R_o$ and $z = -2.0R_o$; blue with blue error bars), as well as the background distribution (green).

Increasing the drift speed in the simulation to $32c_s$ leads to much stronger perturbations to the plasma, as shown in the right half of Figure 2. A density-enhanced electron wing with average velocity away from the obstacle can be seen to originate from the terminator, followed by a density-depleted region with average velocity towards the obstacle. The density-enhanced wing is associated with a much sharper transition to a very negative potential at the terminator, which occurs because the ion flux to the lower half of the obstacle is practically zero at this drift speed. A similar density-enhancement has been observed previously[38], though there for drift at a 45° angle to the magnetic field, which moves the location of the terminator and gives the electrons a parallel drift component.

Ahead of the density-enhanced wing the electron distribution displays similar features to those seen at the slower drift, though as shown in Figure 4 they are more pronounced. In particular, the value of the distribution reached before the cutoff is more or less equal to that at the peak of the background distribution, and the general shift of the distribution towards negative velocities is much more noticeable. A similar general shift is seen in the density-enhanced wing, as shown in Figure 5 (in black and red), though rather than a slope inversion and

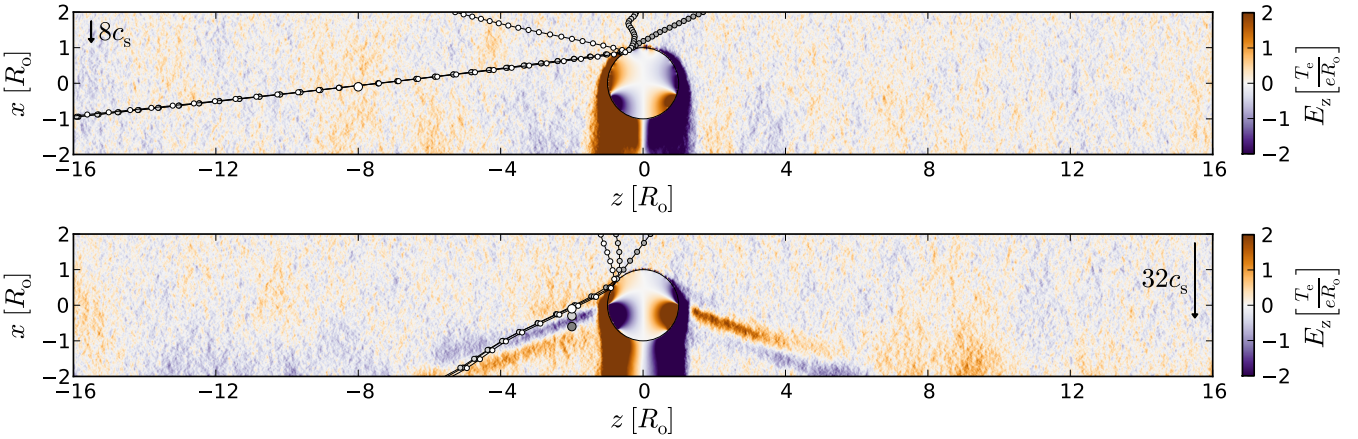

FIG. 6. Parallel electric field E_z and illustrative energized electron trajectories (lines with small circles every 16 time-steps) for drift speeds $8c_s$ (top) and $32c_s$ (bottom) past an insulating obstacle.

a sharp cutoff that distribution has a shoulder and a slow decay that remains above the background distribution at all velocities. Also shown in Figure 5 (in blue) is the distribution in the density-depleted region below the wing, seen to have a general shift towards positive velocities and have a lower value than the background distribution for the velocities where the wing-distribution have a higher value.

Drift-energization is the main mechanism responsible for generating the reversed-slope segments of the electron distributions shown in Figures 3 and 4. To illustrate this mechanism, some example electron trajectories with $v_z < -60c_s$ at the locations of the small white circles in Figure 2 are shown in Figure 6, overlaying the parallel electric field in the corresponding simulation (for which the scale is strongly saturated near the obstacle and in the wake). All three trajectories shown in each set pass near the same location with a similar velocity, so they lie almost on top of each other after interacting with the obstacle surface. Before that interaction however, they have a wide range of parallel velocities, as can be seen from the z-spacing of the circles placed every 16 time-steps on each trajectory. Since the middle trajectory shown for a drift speed of $8c_s$ starts off with near-zero parallel kinetic energy (with its small parallel velocity occasionally changing sign) but ends up with a parallel velocity $v_z < -60c_s$ in a region with near-zero potential, it is clear that drift-energization can add more than T_e/e in kinetic energy to some electrons. This explains how there can be particles present in these simulations with significantly greater velocities than at the same locations in ballistic simulations.

In collisionless plasmas, such as those simulated here, the value of the distribution function is constant along particle trajectories. Since the background distribution is Maxwellian, trajectories with slower initial parallel velocities correspond to higher values of the distribution function, which explains how drift-energization can give values of the observed distribution higher than those of the background distribution at the same final velocities. That trajectories (shown in Figure 6) with such a wide range of initial velocities end up with the very fastest final velocities (near the cutoff) in Figure 3, indicates that there are variations of the distribution function present that are not resolved in the observed distribution. Through such *focusing* of electron trajectories, drift-energization can thus give steep gradients of the distribution function in the forewake, potentially making it unstable.

Though it has been explained how drift-energization can give values of the electron distribution above those of the background distribution at the same velocities, it is not yet clear why the slope of the distribution reverses before the cutoff. One way to arrange such a slope-reversal, is for the energization process to map the slower of two initial velocities to the faster of the corresponding final velocities. However, such details of the energization process are not necessary to give a slope-reversal, since one will arise from a simple geometrical effect: The fastest particles reach farther in z in the same amount of time than slower particles originating from the same energizing region; this means that the value of the distribution will remain higher at larger distances from that region for velocities near the cutoff than for slower velocities. At the slower velocities, the values of the distribution will approach those of the background distribution, since the particles at those velocities far from the obstacle have not interacted with it. The result is a rise in distribution-value just before the velocity-cutoff, implying that a slope-inversion will inevitably occur when the fastest drift-energized particles reach far enough from the obstacle. Further, the reversed slope will steepen farther from the obstacle, eventually making it unstable.

The density-enhanced wing (and trailing density-depletion) seen in the right half (drift speed $32c_s$) of Figure 2 can also be explained by drift-energization. Electrons which encounter the obstacle surface near the terminator see a potential that is quickly becoming more

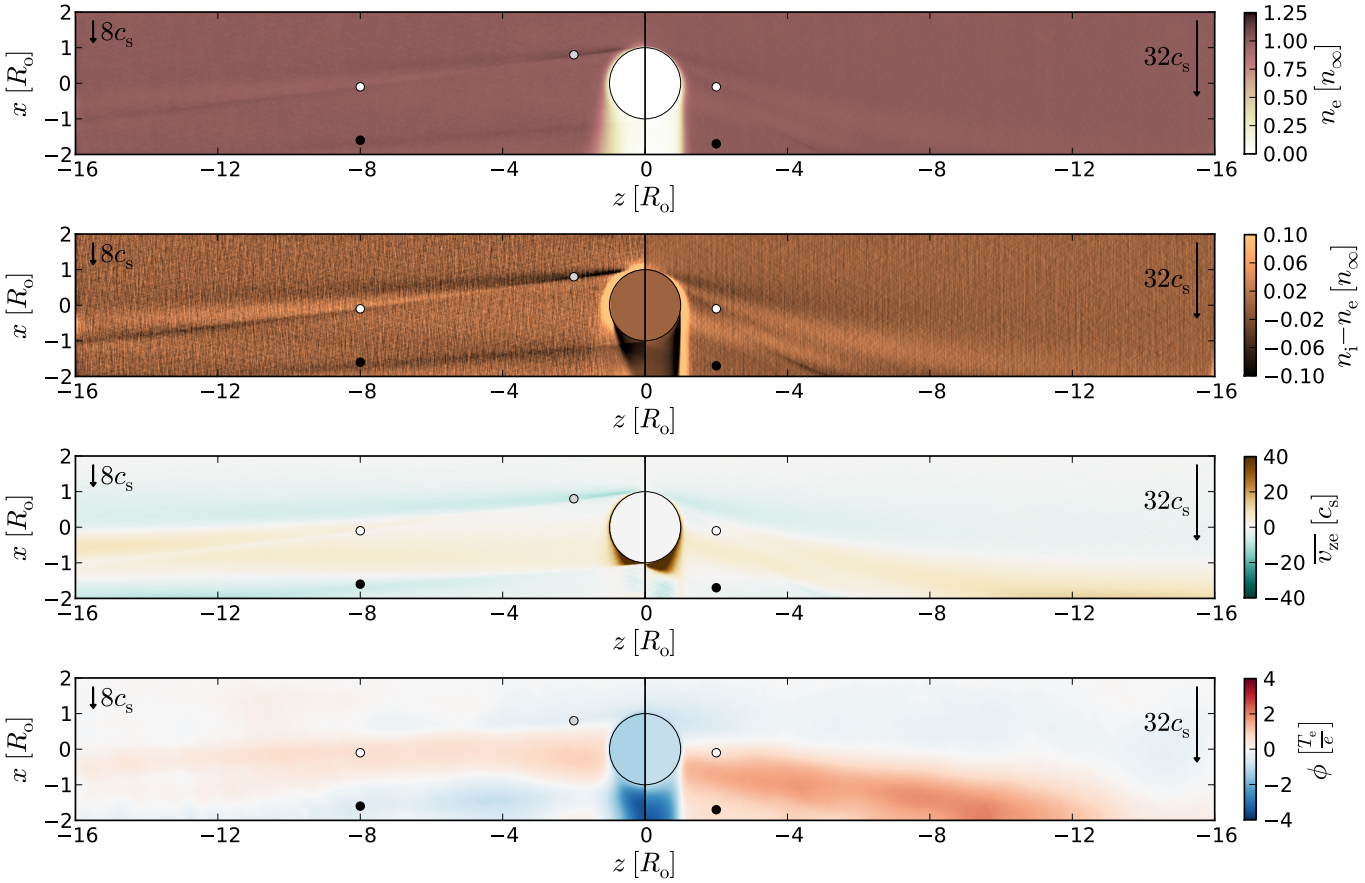

FIG. 7. Plasma drift past a floating-potential conducting obstacle, showing the electron density n_e, normalized charge density $n_i - n_e$, average parallel electron velocity $\overline{v_{ze}}$, and electrostatic potential ϕ for drift speeds $8c_s$ (left) and $32c_s$ (right).

negative in the drift-direction, and therefore energize as they interact with the obstacle. This enhances the density in the wing by giving rise to the shoulder of the electron distribution shown in Figure 5 (in black and red). Meanwhile, the lower values of the distribution in the density-depletion trailing the wing, also shown in Figure 5 (in blue), are a sign of de-energization, presumably taking place as electrons reflect from a region just below the terminator (where the potential is becoming less negative).

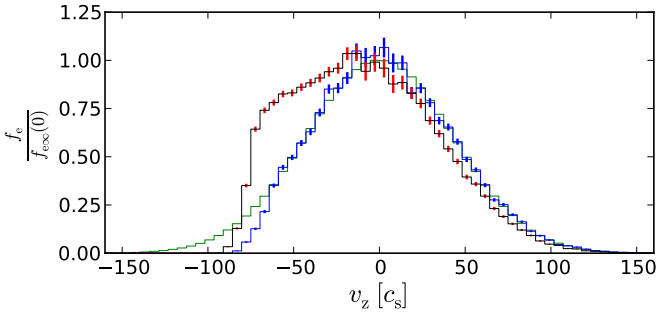

FIG. 8. Parallel electron velocity distribution f_e at the small light-gray circle in Figure 7 ($x = 0.8R_o$ and $z = -2.0R_o$; black with red error bars), and the shadowed electron distribution from the same location in Figure 1 (blue with blue error bars), as well as the background distribution (green).

V. CONDUCTING OBSTACLE

The simulations presented in this section use a uniform floating potential across the entire circular cross-section of the obstacle to balance the electron and ion fluxes to the surface, as described in Section II. This configuration mimics that of a conductor, though the 2D nature of the present simulations means that they are not directly applicable to all conducting obstacles; this is discussed further in Section VI.

In a simulation with drift speed $8c_s$ the floating potential reached by the obstacle is $\phi_o = -1.27^{T_e}/_e$, seen in the left half of Figure 7 to give rise to a density-enhanced wing originating at the top of the obstacle (dark streak with small light-gray circle). That wing resembles the one originating from the terminator in faster flow past an insulator. The electron distribution in the wing (at the small light-gray circle) is shown in Figure 8 (in black and red). Also shown in that figure (in blue) is the electron distribution at the same location but in the simula-

tion only considering shadowing (presented in Figure 1), which shows that the velocity-cutoff from shadowing is smeared out at this location because of the finite spatial-extent of the box for which the distribution is shown. For a wide range of negative velocities, the values of the distribution near the conductor are significantly higher than those of the shadowed distribution, indicating that drift-energization plays a key role in the formation of the density-enhanced wing also in this case.

Drift-energization is typically considered theoretically in the planar approximation, where the de Hoffmann–Teller (dHT) frame[39] allows the energization to be calculated. In that frame the potential structure is stationary, and the motion of the particles is purely parallel to the magnetic field, provided there is planar symmetry in the interaction region. Such symmetry was not present near the surface of the insulator considered in Section IV, since the potential was varying across its surface, but the planar approximation is closer to reality for the uniform floating-potential used in this section, given that the Debye-length is much shorter than the radius of curvature of the surface. The local velocity of the dHT frame is

$$\mathbf{v}_{\mathrm{dHT}} = \mathbf{v}_{\mathrm{d}} - \frac{\mathbf{v}_{\mathrm{d}} \cdot \hat{\mathbf{n}}}{\mathbf{B} \cdot \hat{\mathbf{n}}} \mathbf{B} = v_{\mathrm{d}} \left(-\hat{\mathbf{x}} + \cot\theta \hat{\mathbf{z}} \right) , \qquad (1)$$

where $\mathbf{v}_{\mathrm{d}}$ is the drift velocity, $\hat{\mathbf{n}}$ is the unit normal to the surface, and $\theta = \arcsin\left(\hat{\mathbf{z}} \cdot \hat{\mathbf{n}}\right)$ is the angle between the magnetic field and the tangent to the surface. A circular cross-section like that used in the present simulations provides the full range of surface normals, in principle spanning (at different locations) the full range of parallel dHT velocities for any drift, though in practice the planar approximation likely breaks down near the very top of the obstacle where the denominator $\mathbf{b} \cdot \mathbf{n}$ becomes small.

To be energized, an electron needs to be reflected in the dHT frame. Such reflection can occur only if the parallel kinetic energy of the electron in the dHT frame is less than its potential energy at the obstacle surface, so its parallel speed must be less than $v_{\mathrm{o}} = \sqrt{-2e\phi_{\mathrm{o}}/m_{\mathrm{e}}}$. An electron with initial parallel velocity v_{z}' in the rest frame, reflecting in a dHT frame moving with parallel velocity $v_{\mathrm{dHTz}} = \mathbf{v}_{\mathrm{dHT}} \cdot \hat{\mathbf{z}}$, will then end up with a velocity $v_{\mathrm{z}} = -v_{\mathrm{z}}' + 2v_{\mathrm{dHTz}}$ in the rest frame after reflection, provided $|v_{\mathrm{z}}' - v_{\mathrm{dHTz}}| < v_{\mathrm{o}}$. That corresponds to an energy increase of $m_{\mathrm{e}} v_{\mathrm{dHTz}} \left(2v_{\mathrm{dHTz}} - v_{\mathrm{z}}'\right)$, which is the drift-energization. Rather than use these expressions to calculate the velocity change, that change and the dHT-velocity will be inferred from the simulations, allowing the angle $\theta = \operatorname{arccot}\left(v_{\mathrm{dHTz}}/v_{\mathrm{d}}\right)$ to be calculated. For the circular cross-section considered here θ is also the angle between the x-axis and the normal to the surface, thereby corresponding to a particular location on the surface. Therefore, the location where an electron interacts with the surface should be consistent with the value of θ calculated from its velocity change.

Equipped with the understanding from the dHT frame, it is now useful to re-examine the density-enhanced wing

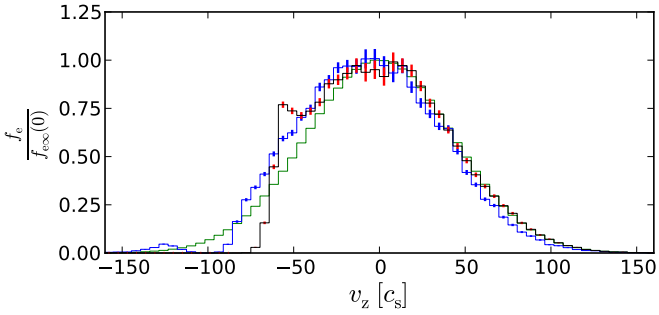

FIG. 9. Parallel electron velocity distribution f_{e} at the left (drift speed $8c_{\mathrm{s}}$) small white circle in Figure 7 ($x = -0.1R_{\mathrm{o}}$ and $z = -8.0R_{\mathrm{o}}$; black with red error bars), and at the left small black circle ($x = -1.6R_{\mathrm{o}}$ and $z = -8.0R_{\mathrm{o}}$; blue with blue error bars), as well as the background distribution (green).

near the top of the obstacle (at the drift speed $8c_{\mathrm{s}}$), for which the electron distribution was contrasted with that from pure shadowing in Figure 8. The distribution in the wing has an excess of electrons for almost all negative velocities, and it is especially large for $v_{\mathrm{z}} \approx -70c_{\mathrm{s}}$. Based on the value of the distribution there it appears those electrons started off with $v_{\mathrm{z}}' \approx \pm 34c_{\mathrm{s}}$, and for now it will be assumed that the negative sign is the correct one. That implies a parallel dHT-frame velocity of $v_{\mathrm{dHTz}} \approx -52c_{\mathrm{s}}$, which corresponds to an angle $\theta = -9°$. It is indeed the case that the electrons will be reflected in that dHT frame, since their initial velocities there ($v_{\mathrm{z}}' - v_{\mathrm{dHTz}} \approx 18c_{\mathrm{s}}$) are well within the maximum speed that can be reflected, which for $\phi_{\mathrm{o}} = -1.27T_{\mathrm{e}}/e$ comes out to $v_{\mathrm{o}} = 68c_{\mathrm{s}}$. Less negative final velocities in Figure 8 have smaller excesses and inferred energizations, but both are still significant at $v_{\mathrm{z}} \approx -50c_{\mathrm{s}}$. For that final velocity the inferred initial velocity is $v_{\mathrm{z}}' \approx \pm 24c_{\mathrm{s}}$, implying a parallel dHT-frame velocity $v_{\mathrm{dHTz}} \approx -37c_{\mathrm{s}}$ (again assuming a negative v_{z}') and an angle $\theta = -12°$. A large fraction of the energized electrons are thus predicted to have interacted with the surface at locations with angles in the range $-12° \lesssim \theta \lesssim -9°$, which seems to correspond well to the extrapolated origin of the density-enhanced wing near the top of the obstacle in Figure 7. Repeating the calculation for the positive values of v_{z}' gives an angle range $-32° \lesssim \theta \lesssim -24°$, which is more difficult to reconcile with Figure 7 (especially since the slower particles would be originating from the more negative values of θ). It thus appears that the density-enhanced wing is mainly associated with particles that start off with a negative parallel velocity v_{z}', and then have that velocity energized to the more negative velocity v_{z} when interacting with the surface near the top of the obstacle.

Looking at the charge density in the left half of Figure 7, a narrow enhancement in electron density is also seen to originate near the bottom of the obstacle. It arises from electrons that pass immediately behind the obstacle, where the potential is less negative than in the rest of the wake because of a transition region from the

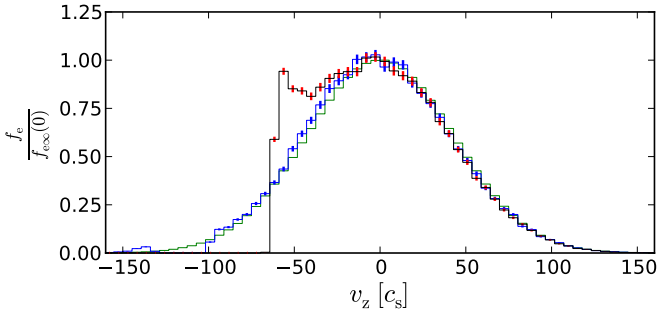

FIG. 10. Parallel electron velocity distribution f_e at the right (drift speed $32c_s$) small white circle in Figure 7 ($x = -0.1R_o$ and $z = -2.0R_o$; black with red error bars), and at the right small black circle ($x = -1.7R_o$ and $z = -2.0R_o$; blue with blue error bars), as well as the background distribution (green).

surface potential to the wake potential; that transition lets electrons through that would otherwise be reflected by the very negative wake potential. At the upper edge of this density-enhancement the electron distribution has a bump at highly negative velocities, as shown (in blue) in Figure 9 for the location of the left small black circle in Figure 7. The bump has distribution values higher than the background distribution at the fastest velocities, indicating that the corresponding trajectories have been drift-energized. Below the density-enhancement the distribution (not shown) qualitatively matches that expected from drift de-energization[14], having a notch at the boundary between reflected and passing particles.

Also shown in Figure 9 (in black and red) is the distribution at the location of the left white circle in Figure 7, which is the same location as that examined in Figure 3 for the insulating obstacle (the white circles in Figure 7 are the same as those in Figure 2). A slope-reversal and velocity-cutoff of the distribution are present also for the conducting obstacle, similar to those seen for the insulating one. The distribution quickly becomes more Maxwellian as moving farther down into the conductor forewake, but because the surface potential does not become more negative the cutoff-location doesn't shift as far towards negative velocities as it does for the insulating obstacle. The cutoff remains as the interaction-point moves below the terminator, and can even be seen (at $v_z \approx -90c_s$ in blue in Figure 9) where electrons appear that have passed behind the obstacle.

Increasing the flow speed to $32c_s$ largely (though not entirely) eliminates the density-enhancements seen for slower flow, as shown in the right half of Figure 7. The floating potential has been reduced to $\phi_o = -0.94T_e/e$, which reduces the maximum speed in the dHT frame to $v_o = 59c_s$, and the faster drift makes all dHT-implied angles larger in magnitude since $\theta = \text{arccot}\,(v_{dHTz}/v_d)$. Electron shielding of the potential near the top of the obstacle is also less efficient at this fast drift, as evident from the absence of charge-density there, perhaps rendering the planar dHT approximation less applicable there. The net result is less effective and more diffuse energization, which does not give rise to a strongly density-enhanced wing. However, farther down on the obstacle surface, drift-energization does still occur, and as seen in Figure 10 both the main electron-distribution modifications discussed for the slower drift are still present; there is a distinct bump of electrons passing behind the obstacle at large negative velocities at the one location (in blue), and a slope-reversal before the cutoff at the other (in black and red). Note that the velocity-cutoff of the blue curve in Figure 10 (drift speed $32c_s$) is at a more negative velocity than that in Figure 9 (drift speed $8c_s$), despite the floating potential being less negative at the faster drift. This is in part because the corresponding electrons have been reflected off the wake, rather than the obstacle surface, but also because there is a positive potential at the location of the black circle for the faster drift.

Some example electron trajectories with $v_z < -60c_s$ at the locations of the small white circles in Figure 7 are shown in Figure 11, overlaying the parallel electric field in the corresponding simulations (for which the scale is strongly saturated near the obstacle and in the wake). The trajectories for drift speed $32c_s$ are similar to those shown for the insulating case in Figure 6, though only a narrow range of initial parallel velocities near $v_z' = 0$ appear to be energized to $v_z < -60c_s$ at the white circle. Their interaction-locations with the surface nicely match the dHT-frame interpretation, which implies an angle $\theta = -46°$. Further, the near-zero initial velocity is consistent with the value of the distribution near the velocity-cutoff in Figure 10 (in black and red), which is close to that of the background distribution at zero velocity. At the slower drift speed $8c_s$ the three example trajectories through the white circle each interact with the surface at a different location, and each experience a different level of energization. As expected from the dHT-interpretation, the level of energization of those trajectories is largest for the least negative values of θ.

Also shown in Figure 11 are some trajectories passing through the small black circles in Figure 7, for particles that have passed behind the obstacle and are part of the bump in the electron distribution. These trajectories all start off with highly negative velocities, and appear to have their parallel kinetic energy increased further while moving through the wake. For drift speed $32c_s$, part of that increase is likely the result of the positive potential at the location of the corresponding black circle, making it more difficult to isolate the effect of drift-energization, but for drift speed $8c_s$ it is clear that drift-energization is responsible for boosting the velocity of the bump. This energization takes place as electrons pass through the potential structure immediately trailing the obstacle, where the potential is becoming more negative as it transitions from the obstacle potential to the wake potential. First, the electrons are slowed down somewhat as they encounter a repelling electric field at the edge of the wake. Second, they see an electric field accelerating them towards the axis of symmetry. Third,

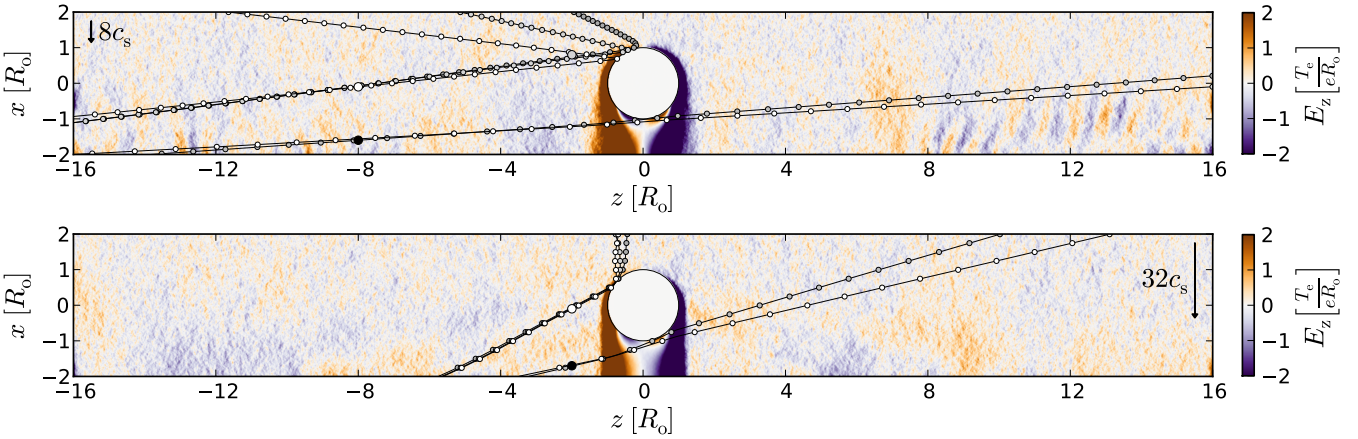

FIG. 11. Parallel electric field E_z and illustrative energized electron trajectories (lines with small circles every 16 time-steps) for drift speeds $8c_s$ (top) and $32c_s$ (bottom) past a floating-potential conducting obstacle.

they encounter a weaker field decelerating them on the other side of that axis, because they have drifted farther from the obstacle. And finally, the electrons encounter a larger potential drop accelerating them out of the wake than that which initially slowed them down when entering it, again since the influence of the obstacle on the potential has gotten weaker. The net result is thus that the transition-region of the potential behind the obstacle is able to energize these electrons.

The parallel electric field in Figure 11 shows evidence of some wave-like fluctuations near the domain boundary for drift speed $8c_s$. These fluctuations did not show up clearly in Figure 7, since each density and average parallel velocity plot thus far has been averaged over 128 time-steps. To further examine the fluctuations, two simulations were run with a domain twice as large in each dimension, with roughly 3×10^8 particles of each species, and with the obstacle potentials fixed at the previously established floating potentials ($\phi_o = -1.27T_e/e$ for drift speed $8c_s$ and $\phi_o = -0.94T_e/e$ for drift speed $32c_s$). The instantaneous quantities for a single time-step are shown in Figure 12, and clear wave-like perturbations are now seen in each of the quantities in both simulations. The parallel wave-lengths are $\sim 10\lambda_{De}$ for drift speed $8c_s$ and $\sim 16\lambda_{De}$ for drift speed $32c_s$, and the waves propagate outward with speeds $\sim 110c_s$. (It was verified that the characteristics of the perturbations are not sensitive to the size of the time-step, and repeating the simulation with a zero-gradient boundary condition for the potential at the left and right boundaries led to a similar result.) The observed propagation velocities suggest that the perturbations are the result of electron two-stream instabilities, associated with the gaps in the distributions shown in Figures 9 and 10 (in blue).

VI. DISCUSSION

Sections IV and V have illustrated the electron distribution modifications that can result from shadowing, space-charge, and drift-energization for a small subset of a vast parameter space. How widely such phenomena apply will ultimately need to be explored with further simulations, but some discussion of when the present simulations may directly apply and where similar phenomena may arise is presented here.

For insulating obstacles the present 2D simulations apply quite generally in the parameter regime studied, provided the extent of the obstacle in the ignorable direction is much larger than the typical electron gyroradius. However, the insulating boundary-conditions used (described in Section II) do not include effects such as photoemission, secondary emission, or reflection of electrons by local magnetic field structures near the surface (e.g. Ref. 40), which for example can be important for obstacles in the solar wind. Such effects could lead to modifications of the electron distribution by altering the absorption efficiency and introducing electrons at different energies, but regardless of the details, the net charge of electrons and of ions removed from a dense flowing plasma should be approximately equal everywhere on the insulator surface. The boundary conditions used presently thus capture the right overall impact of the obstacle on the plasma, so it is expected that drift-energization and the main features of the electron distribution discussed in Section IV would be present even if other emission or reflection processes play a role near the surface.

In the case of a conducting obstacle (or an insulating one with a conducting core), the direct applicability of 2D simulations is more limited. This is because a conductor will shield the background electric field driving the $\mathbf{E}\times\mathbf{B}$ drift, or (equivalently) have an electric field induced in it if moving through a magnetic field. The plasma will counteract such shielding, giving rise to a transition region over which the external $\mathbf{E}\times\mathbf{B}$ drift decays while local

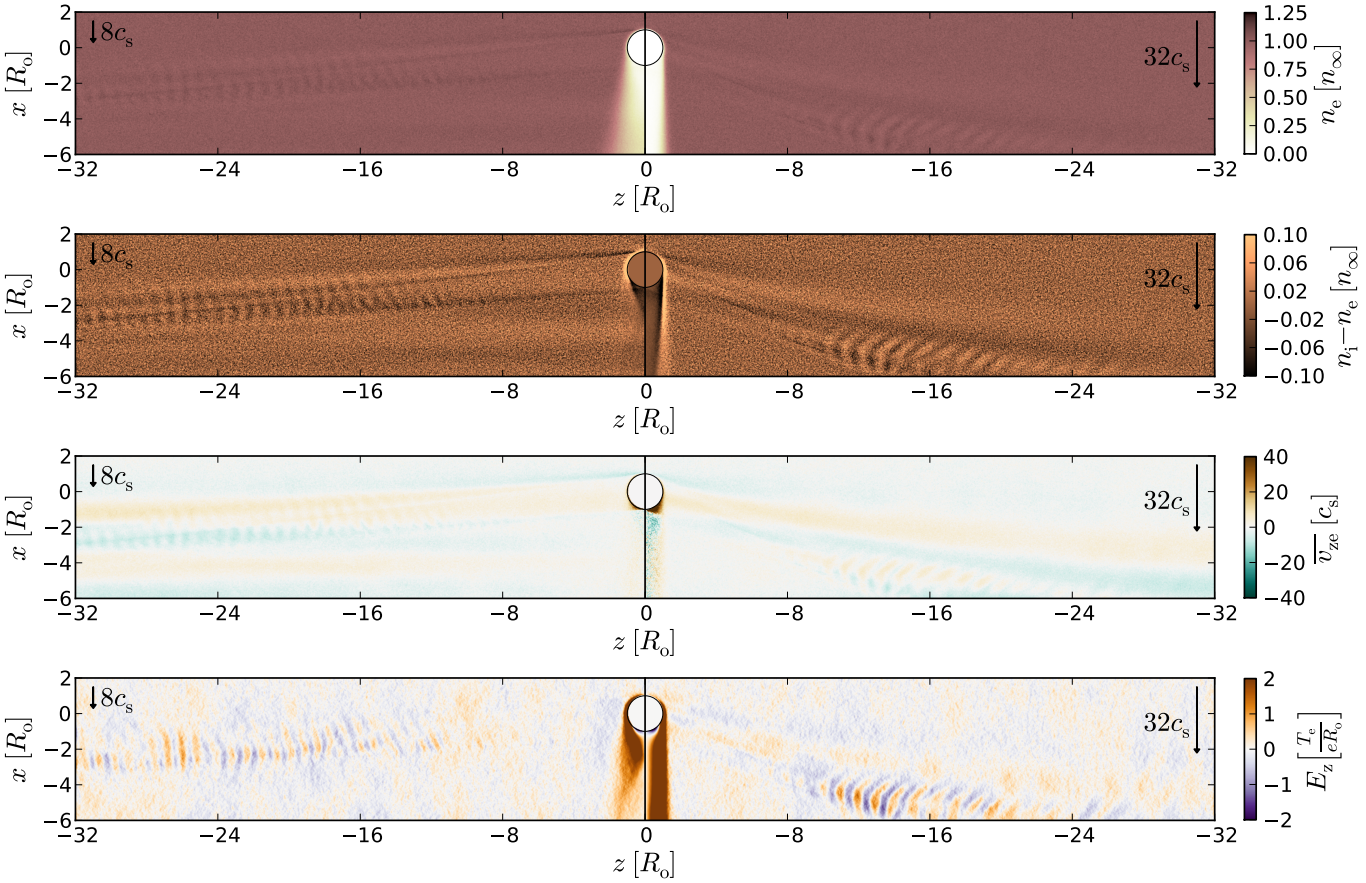

FIG. 12. Instantaneous electron density n_e, normalized charge density $n_i - n_e$, average parallel electron velocity $\overline{v_{ze}}$, and electrostatic potential ϕ of a plasma drifting past a floating-potential conducting obstacle, for drift speeds $8c_s$ (left) and $32c_s$ (right).

ones arise[31]. This will be an inherently 3D configuration, where it is difficult to say *a priori* how drift-energization will differ from that seen in the 2D simulations presented in Section V.

Beyond the specific applications of the present simulations, it is interesting to ask more generally when drift-energization might be important, and how varying the plasma parameters would affect it. Going to a shorter Debye-length is likely to weaken the density-enhanced wings observed in some of the simulations, since such charge-separation is more difficult to sustain in a dense plasma. More effective shielding will also shrink the potential structure near the terminator driving the wing-generation in the insulating case, weakening it further. In contrast, shrinking the sheath-like layer on the top surface of the obstacle is likely to make the planar approximation more applicable, giving robust dHT-frame energization. Further, sufficiently short Debye-lengths are likely to make the planar approximation also hold for insulating obstacles, since the potential variation across the surface will be negligible on the shielding-scale. The reversed-slope feature of the electron distribution observed in each of the simulations is thus expected to be present also in the limit of short Debye-length, suggesting that drift-energization quite robustly modifies the electron distribution in the studied drift-range. Shorter Debye-lengths will also give faster growth-rates of any instabilities, potentially leading to an unsteady forewake also for the insulating obstacle.

At slower drift speeds, is likely that drift-energization can still take place near the top of the obstacle, since there are still dHT-frames there with any required velocity, but the limited angle range over which energization can take place and possible breakdown of the dHT approximation are expected to eventually make drift-energization unimportant. Another point is that a typical ion-gyroradius larger than the Debye length will alter the potential structure near the obstacle at slow drifts, possibly interfering with drift-energization by altering the perpendicular scale of the energizing potential. Only purely perpendicular plasma drift has been considered in the present simulations, but a large parallel drift component (comparable to the electron thermal velocity) could also affect drift-energization and the forewake; smaller parallel drifts are likely to simply perturb the phenomena observed here.

Inherent to the present simulations is the assumption that the gyroradii of the electrons are smaller than the

scale of potential structures arising from the obstacle. In some physical systems, like the moon in the solar wind, the ordering is reversed, with the Debye-length being much smaller than the typical gyromotion scale. That is a very different regime than the one studied here, and can lead to enhancement of the perpendicular kinetic energy of electrons rather than the parallel one. In that limit reflection off crustal magnetic fields near the lunar surface[40] provide an alternative electron-reflection mechanism to negative charging, and such reflection produces a loss-cone in the electron distribution, appearing as a conic in the solar-wind frame[41,42]. Similar energy-dependent features would likely arise from reflection by electrostatic structures, leading to much more complicated distribution modifications than the clean drift-energization considered here.

VII. CONCLUSIONS

The electron *forewake* has been explored with fully kinetic PIC simulations, revealing the importance of drift-energization in establishing modifications to the electron distribution in some regions. More generally, the inclusion of the effects of space-charge and surface-charging in a self-consistent simulation have elucidated where and when distribution modifications predicted from non self-consistent calculations[14,23] are present. This work represents a large step in understanding over previous simulations, which either used an artificial mass ratio[37], ignored the magnetic field[43], or didn't discover distribution-modifications beyond those evident in the density[38].

Three main features of the forewake electron distribution have been discussed: a seemingly robust slope-inversion resulting from drift-energization at the top half of the obstacle; more specific density-enhanced wings originating from the top of a conductor at drift speed $8c_s$ and from the terminator of an insulator at drift speed $32c_s$; and a bump from particles passing behind a conducting obstacle, separated from the rest of the distribution by a gap. The first of these is expected to persist to shorter Debye lengths, appears to be insensitive to the boundary condition at the surface, and should eventually become unstable because it steepens as faster particles lead slower ones in space. The other two are likely more specific to the present simulations, and are expected to diminish if the Debye-length is made shorter or the obstacle surface-potential is altered. This means that the instability presently observed for flow past a conductor may be limited to certain parameter regimes, making it all the more interesting that the more robust slope-reversal from drift-energization could make the forewake unstable. Such instability would indeed earn the forewake its name, strengthening the analogy to the Earth's *foreshock*.

Though the present results for an insulating obstacle have quite wide applicability, the 2D nature of the simulations is more limiting for conducting obstacles. To truly characterize drift-energization near a conductor thus requires 3D simulations, which will prove even more computationally demanding than the large parallel simulations carried out here. Conducting Mach-probes are also typically used to measure slower drifts than those considered presently, further increasing the cost of such simulations by requiring them to follow wider domains for longer time-durations. The added insight would be great however, as negatively biased probes could then be simulated, allowing the impact of forewake phenomena on the measured probe signals to be realistically assessed.

ACKNOWLEDGMENTS

C. B. Haakonsen was supported by NSF/DOE Grant No. DE-SC0010491. Computer simulations using COPTIC were carried out on the MIT PSFC parallel AMD Opteron/Infiniband cluster Loki.

[1] J. Halekas, Y. Saito, G. Delory, and W. Farrell, Planetary and Space Science **59**, 1681 (2011).
[2] N. Smick, B. LaBombard, and I. Hutchinson, Nuclear Fusion **53**, 023001 (2013).
[3] P. Israelevich and L. Ofman, Journal of Geophysical Research **117**, A08223 (2012).
[4] P. Trávníček, Geophysical Research Letters **32**, L06102 (2005).
[5] E. Kallio, Geophysical Research Letters **32**, L06107 (2005).
[6] Y.-C. Wang, J. Müller, W.-H. Ip, and U. Motschmann, Icarus **216**, 415 (2011).
[7] S. Wiehle, F. Plaschke, U. Motschmann, K.-H. Glassmeier, H. Auster, V. Angelopoulos, J. Mueller, H. Kriegel, E. Georgescu, J. Halekas, D. Sibeck, and J. McFadden, Planetary and Space Science **59**, 661 (2011).
[8] M. Holmström, S. Fatemi, Y. Futaana, and H. Nilsson, Earth, Planets and Space **64**, 237 (2012).
[9] W. M. Farrell, M. L. Kaiser, J. T. Steinberg, and S. D. Bale, Journal of Geophysical Research **103**, 23653 (1998).
[10] W. M. Farrell, T. J. Stubbs, J. S. Halekas, G. T. Delory, M. R. Collier, R. R. Vondrak, and R. P. Lin, Geophysical Research Letters **35**, L05105 (2008).
[11] P. C. Birch and S. C. Chapman, Physics of Plasmas **8**, 4551 (2001).
[12] P. C. Birch and S. C. Chapman, Physics of Plasmas **9**, 1785 (2002).
[13] C. B. Haakonsen, I. H. Hutchinson, and C. Zhou, Physics of Plasmas **22**, 032311 (2015).
[14] I. H. Hutchinson, Journal of Geophysical Research **117**, A03101 (2012).
[15] I. H. Hutchinson, C. B. Haakonsen, and C. Zhou, Physics of Plasmas **22**, 032312 (2015).
[16] C. Hines, Planetary and Space Science **10**, 239 (1963).
[17] B. U. O. Sonnerup, Journal of Geophysical Research **74**, 1301 (1969).
[18] L. Ball and D. B. Melrose, Publications of the Astronomical Society of Australia **18**, 361 (2001).
[19] R. J. Fitzenreiter, J. D. Scudder, and A. J. Klimas, Journal of Geophysical Research **95**, 4155 (1990).
[20] P. C. Filbert and P. J. Kellogg, Journal of Geophysical Research **84**, 1369 (1979).
[21] K. A. Anderson, R. P. Lin, F. Martel, C. S. Lin, G. K. Parks, and H. Rème, Geophysical Research Letters **6**, 401 (1979).
[22] W. M. Farrell, R. J. Fitzenreiter, C. J. Owen, J. B. Byrnes, R. P. Lepping, K. W. Ogilvie, and F. Neubauer, Geophysical Research Letters **23**, 1271 (1996).
[23] S. D. Bale, Journal of Geophysical Research **102**, 19773 (1997).

[24]S. D. Bale, C. J. Owen, J.-L. Bougeret, K. Goetz, P. J. Kellogg, R. P. Lepping, R. Manning, and S. J. Monson, Geophysical Research Letters **24**, 1427 (1997).
[25]I. H. Hutchinson, Physics of Fluids **30**, 3777 (1987).
[26]H. Van Goubergen, R. R. Weynants, S. Jachmich, M. Van Schoor, G. Van Oost, and E. Desoppere, Plasma Physics and Controlled Fusion **41**, L17 (1999).
[27]P. Peleman, S. Jachmich, M. Schoor, and G. Oost, Czechoslovak Journal of Physics **55**, 381 (2005).
[28]I. H. Hutchinson, Physical Review Letters **101**, 035004 (2008).
[29]I. H. Hutchinson, Physics of Plasmas **15**, 123503 (2008).
[30]L. Patacchini and I. Hutchinson, Physical Review E **80**, 036403 (2009).
[31]L. Patacchini, *Collisionless ion collection by non-emitting spherical bodies in E x B fields*, Ph.D. thesis, Massachusetts Institute of Technology (2010).
[32]L. Patacchini and I. H. Hutchinson, Plasma Physics and Controlled Fusion **52**, 035005 (2010).
[33]L. Patacchini and I. H. Hutchinson, Plasma Physics and Controlled Fusion **53**, 025005 (2011).
[34]L. Patacchini, I. H. Hutchinson, and G. Lapenta, Physics of Plasmas **14**, 062111 (2007).
[35]I. H. Hutchinson, Physics of Plasmas **18**, 032111 (2011).
[36]C. K. Birdsall and A. B. Langdon, *Plasma physics via computer simulation* (Adam Hilger, Bristol, 1991).
[37]T. Umeda, T. Kimura, K. Togano, K. Fukazawa, Y. Matsumoto, T. Miyoshi, N. Terada, T. K. M. Nakamura, and T. Ogino, Physics of Plasmas **18**, 012908 (2011).
[38]T. Nakagawa and S. Kimura, Earth, Planets and Space **63**, 477 (2011).
[39]F. De Hoffmann and E. Teller, Physical Review **80**, 692 (1950).
[40]D. Mitchell, J. Halekas, R. Lin, S. Frey, L. Hood, M. Acuña, and A. Binder, Icarus **194**, 401 (2008).
[41]J. S. Halekas, A. R. Poppe, W. M. Farrell, G. T. Delory, V. Angelopoulos, J. P. McFadden, J. W. Bonnell, K. H. Glassmeier, F. Plaschke, A. Roux, and R. E. Ergun, Journal of Geophysical Research **117**, A05101 (2012).
[42]J. S. Halekas, A. Poppe, G. T. Delory, W. M. Farrell, and M. Horanyi, Earth Planets Space **64**, 73 (2012).
[43]S. Kimura and T. Nakagawa, Earth, Planets and Space **60**, 591 (2008).